International Journal of Power Electronics and Drive System (IJPEDS)
Vol. 17, No. 4, December 2026, pp. 2891~2902
ISSN: 2088-8694, DOI: 10.11591/ijpeds.v17.i4.pp2891-2902

Observer-based sliding mode control for high-gain boost converters in renewable systems

Thanh-Lam Le, Nguyen Nhan Bon
Faculty of Electrical and Electronics Engineering, Ho Chi Minh City University of Technology and Engineering, Ho Chi Minh City, Vietnam

Article Info

Article history:

Received Jun 28, 2026
Revised Aug 28, 2026
Accepted Sep 13, 2026

Keywords:

Anti-windup control
Disturbance rejection
High-gain DC-DC converter
Linear extended-state observer
Output-feedback regulation
Super-twisting sliding-mode control

ABSTRACT

Robust output-voltage regulation of high-gain capacitor-based boost converters is complicated by coupled internal energy-transfer dynamics, uncertain duty-to-output gain, source and load variations, and sensitivity to switching noise. To address these effects using the output voltage as the sole measured feedback variable, a linear extended-state-observer-assisted integral super-twisting sliding-mode controller (LESO–ISTSMC) is developed from the exact duty-affine output channel of the full averaged model. A second-order LESO estimates the lumped output-channel disturbance from the measured voltage and applied duty ratio, while a tanh-regularized super-twisting law, duty projection, and model-consistent anti-windup feedback produce a continuous commanded-duty correction before PWM realization; under the invariant-region condition stated explicitly in Assumption 1, regional Lyapunov analysis establishes bounded closed-loop signals and an explicit practical regulation bound. Experiments on a TMS320F28379D platform show that, relative to a conventional sign-based sliding-mode controller (CSMC), LESO–ISTSMC reduces normalized reference-centered RMS voltage deviation by 59.75–63.14% over 30–80 V and load-step voltage-dip magnitude by 71.4–85.0% following a 50% load increase. During 48–108 V reference steps at an approximately 24-V input, the converter exhibits well-damped transitions and a mean efficiency of 92.40%, supporting the practical realizability of the output-feedback architecture over the tested operating region.

This is an open access article under the CC BY-SA license.

Corresponding Author:

Thanh-Lam Le
Faculty of Electrical and Electronics Engineering
Ho Chi Minh City University of Technology and Engineering
Ho Chi Minh City, Vietnam
Email: lamlethanh@hcmute.edu.vn

1. INTRODUCTION

The rapid deployment of photovoltaic generation, fuel cells, battery storage, and DC microgrids is shifting DC-DC conversion research from nominal voltage gain toward compact, high-density interfaces that can sustain wide operating ranges. Recent surveys identify high-gain, multiport conversion as a central enabling technology for renewable-energy integration [1]. At the topology level, this trend has produced single-switch step-up converters with moderate duty ratios [2], families with reduced semiconductor voltage stress [3], and coupled-inductor/voltage-multiplier structures designed for low input-current ripple [4]. Multistage capacitor-assisted conversion has also been combined with cascaded PI regulation for low-voltage sources [5], while transformerless quadratic architectures have incorporated component-stress and reliability considerations [6]. Coupled-inductor multiplier cells can further increase gain without an extreme duty ratio [7], and compact single-switch realizations offer continuous input current for photovoltaic interfaces [8].

These developments improve static conversion capability, but they also introduce several interacting capacitor voltages, mode-dependent charge paths, and operating-point-dependent duty authority. Consequently, satisfactory open-loop gain, efficiency, or device stress does not by itself guarantee output-voltage quality when the source, load, and parasitic losses vary. The central challenge addressed here is therefore to achieve robust output-voltage regulation using output feedback while retaining the converter's internal energy-transfer dynamics, rather than replacing them with an idealized static conversion-ratio model.

Control research has accordingly moved from fixed-gain small-signal loops toward nonlinear and disturbance-resilient designs. A recent review of sliding-mode control in power converters emphasizes its robustness to matched uncertainty, while identifying chattering, variable switching activity, and implementation constraints as persistent issues [9]. Feedback-linearizing control has been used to preserve soft-switching operation in quasi-resonant converters [10], and hybrid super-twisting/backstepping designs have stabilized boost converters supplying constant-power loads [11]. For capacitor-diode ladder converters, robust backstepping sliding-mode regulation improves transient performance but retains a model-dependent recursive construction [12]. Disturbance-observer-assisted passivity control offers large-signal stability for dc microgrids [13], whereas dual-loop terminal/super-twisting schemes regulate floating interleaved boost converters at the cost of current-loop sensing and additional controller states [14]. Composite feedback-linearization and nonsingular terminal sliding-mode designs have also been validated experimentally for dc-bus stabilization [15]. More recently, current-sensorless sliding-mode regulation has reduced the sensing burden by estimating the voltage derivative and lumped uncertainty, although the reported verification is simulation-based [16]. Collectively, these studies confirm the value of nonlinear robustness, but they do not remove the practical trade-off: the conventional sign-based sliding-mode controller (CSMC) is simple and robust, yet its discontinuous correction transfers sampling noise and switching uncertainty directly into the duty command; more elaborate alternatives often require extra measurements, an accurate coordinate transformation, or substantial online computation.

Observer-assisted control provides a promising route through this trade-off because uncertainties can be reconstructed before the robust term is asked to dominate them. A linear extended-state observer (LESO) has been combined with sliding-mode control for buck–boost converters with mismatched disturbances [17], while structurally adaptive extended-state observers have improved the disturbance-rejection/noise-suppression compromise in predictive control of bidirectional converters [18]. LESO-based model-free predictive control has likewise been demonstrated on two-stage AC–DC–DC conversion [19], and adaptive fuzzy observers have been used for fault-tolerant boost-converter regulation [20]. The broader observer literature nevertheless shows that high gain cannot be increased without regard to measurement noise: smooth high-gain observers exhibit an explicit bandwidth–noise compromise [21], enhanced LESOs use additional internal models to recover rapidly varying quantities [22], and experimental LESO-assisted adaptive sliding-mode control remains application-specific [23]. Switched-gain observers address the same conflict by separating transient and steady-state gains, but require a switching logic and invariant-set design [24]; offline metaheuristic tuning can improve converter parameters, although it does not reconstruct time-varying disturbances online [25]. Recent converter studies have therefore begun to combine finite-time observers with generalized super-twisting control [26] or smooth-gain sliding laws with reduced-order disturbance estimation [27]. Adaptive super-twisting control has also shown experimentally that continuous higher-order action can mitigate chattering [28], and modified super-twisting laws have been applied to photovoltaic flyback converters [29]. Finite-time unknown-input observers provide a rigorous alternative when the required structural conditions are available [30]. What remains unresolved is an experimentally verified design that i) preserves the exact duty-affine output channel of a high-gain multi-capacitor converter, ii) uses only output voltage and the duty ratio already available in the processor, iii) smooths both super-twisting channels without claiming exact finite-time convergence, and iv) treats duty projection and windup within the stability argument rather than as implementation afterthoughts.

To close this gap, this study develops a linear extended-state-observer-assisted integral super-twisting sliding-mode controller (LESO–ISTSMC) for the high-gain capacitor-based boost converter in Figure 1. The full-order averaged model is retained, while the measured output channel is reformulated by exactly lumping unmeasured energy-storage dynamics, parameter dispersion, source/load variation, and input-gain mismatch; a second-order LESO then estimates the output derivative and total disturbance from output voltage and applied duty ratio. An integral sliding coordinate, tanh-regularized super-twisting law, duty projection, and anti-windup feedback are combined with a regional Lyapunov analysis establishing conditional boundedness and a computable practical regulation bound. The smoothing width affects local reaching dynamics but not the continuous-time asymptotic bound. Implemented on a TMS320F28379D DSP and compared with CSMC under identical hardware conditions, LESO–ISTSMC reduces normalized RMS voltage deviation by 59.75–63.14% over 30–80 V and load-step dips by 71.4–85.0%, while 48–108 V operation achieves 92.40% mean efficiency.

2. CONTROL-ORIENTED MODEL AND PROBLEM FORMULATION

The converter considered in this study is the high-gain capacitor-based boost converter shown in Figure 1. Its energy-storage variables are collected in the state vector $x = [i_L, v_a, v_b, v_1, v_2, v_3]^{\mathrm{T}}$, where i_L is the input-inductor current and v_a, v_b, and v_j $(j = 1,2,3)$ are the voltages across C_a, C_b, and C_j, respectively. Because C_1 and C_3 are series-connected across the load, the regulated voltage is $v_o = v_1 + v_3$. Continuous-conduction operation is assumed within the diode-conduction sequence associated with the stated operating region. The switch and diodes are ideal in the nominal circuit description, whereas conduction losses, dead time, parameter dispersion, and unmodeled commutation effects are retained in an exogenous term rather than discarded from the control model. Within this CCM conduction sequence, the two switch subintervals admit the compact representation.

$$\dot{x} = A_q(R)x + B_q V_g + E_q w, \quad v_o = C_o x, \quad q \in \{0,1\}, \quad C_o = [0 \quad 0 \quad 0 \quad 1 \quad 0 \quad 1] \tag{1}$$

Where $q = 1$ and $q = 0$ denote the on- and off-subintervals, respectively, R is the load resistance, V_g is the input voltage, w collects exogenous and parasitic effects, and $A_q(R)$, B_q, and E_q are the topology-dependent state, source, and disturbance matrices obtained directly from Kirchhoff's laws. This representation retains the complete set of energy-storage states; no capacitor-voltage balancing relation or quasi-steady current approximation is imposed. Let the switching period be much shorter than the dominant electrical time constants. State-space averaging then gives (2).

$$\dot{x} = A(D_a, R)x + B(D_a)V_g + E(D_a)w, \quad D_a \in \mathcal{D} := [D_{\min}, D_{\max}] \subset (0,1) \tag{2}$$

Where D_a is the duty ratio actually applied to the pulse-width modulator, $A(D_a, R) = A_0(R) + D_a[A_1(R) - A_0(R)]$, $B(D_a) = B_0 + D_a(B_1 - B_0)$, and $E(D_a) = E_0 + D_a(E_1 - E_0)$. The interval $\mathcal{D}$ is imposed by the gate driver and provides finite on- and off-times. The (2), rather than a steady-state conversion ratio, is the model used for the subsequent control development.

Pre-multiplication of (2) by C_o exposes the exact duty-affine output channel of the averaged model.

$$\dot{v}_o = a_o(x, V_g, R, w) + b_o(x, V_g, R, w)D_a \tag{3}$$

Where $a_o = C_o[A_0(R)x + B_0 V_g + E_0 w]$ and $b_o = C_o\{[A_1(R) - A_0(R)]x + (B_1 - B_0)V_g + (E_1 - E_0)w\}$. The internal capacitor and inductor dynamics have not disappeared from (3); they enter through a_o and b_o. The representation is therefore local to an operating region in which the duty-to-output direction does not change sign. It does not invoke global input-output linearization and does not require a claim of globally stable zero dynamics. The need to state the operating domain explicitly is consistent with the local linearizing-output construction used for nonminimum-phase converter variables [17].

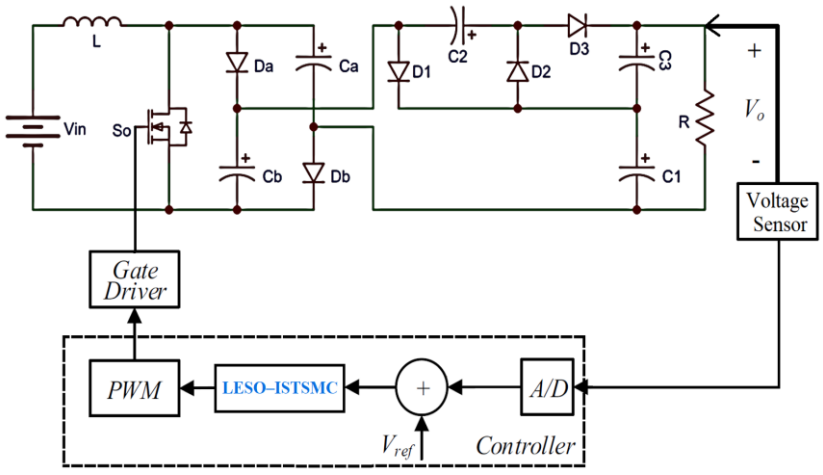

Figure 1. Configuration of the high-gain capacitor-based boost converter and the proposed LESO–ISTSMC voltage-control loop

Choose a nonzero nominal input coefficient b_n with the same sign as b_o. Adding and subtracting $b_n D_a$ converts (3), without approximation, into (4).

$$\dot{v}_o = b_n D_a + d,\ d := a_o + (b_o - b_n) D_a. \tag{4}$$

Where d is the total output-channel disturbance. It contains load and source variations, parasitic losses, interconnection with the unmeasured energy-storage states, and uncertainty in the duty-to-output gain. This definition is important: d is not asserted to be a physically matched disturbance in the original switched circuit. It is an exact lumping in the scalar output channel and is the quantity to be estimated by the observer.

2.1. Assumption 1 (admissible operating region)

The exogenous signal belongs to a compact set $w \in \mathcal{W}$. There exists a compact admissible set $\mathcal{X}$ containing the tested operating points and positively invariant for all admissible $V_g \in [V_g^-, V_g^+]$, $R \in [R^-, R^+]$, $w \in \mathcal{W}$, and $D_a \in \mathcal{D}$, on which the averaged model is well posed. Moreover, b_o has a known constant sign and satisfies $0 < b_- \leq |b_o(x, V_g, R, w)| \leq b_+$, and b_n is selected with that sign. Boundedness of the converter states in the subsequent analysis is therefore conditional on operation in $\mathcal{X}$. Assumption 1 is a regional controllability requirement, not a global property of a boost-derived converter. It excludes duty ratios at which the output channel loses control authority and is physically enforced by the duty limits, component ratings, and the stated voltage range. Accordingly, the closed-loop conclusions below apply only to trajectories initialized and maintained in this admissible region. Introduce $z_1 = v_o$, the extended state $z_2 = d$, and $z = [z_1, z_2]^{\mathrm{T}}$. With the measured voltage y_m, the output channel becomes (5).

$$\dot{z}_1 = b_n D_a + z_2, \quad \dot{z}_2 = h, \quad y_m = z_1 + n. \tag{5}$$

Where $h = \dot{d}$ and n is the voltage-sensor and quantization noise. The formulation uses only the measured output voltage and the duty ratio already available inside the digital controller; no inductor-current sensor is required by the feedback law.

2.2. Assumption 2 (regularity of exogenous signals)

The reference v_r is continuously differentiable and both v_r and $\dot{v}_r$ are bounded; step commands are therefore passed through a bounded-slope reference filter before entering the control law. The total disturbance is locally absolutely continuous and satisfies $|d(t)| \leq d_{\max}$ and $|h(t)| \leq h_{\max}$. The sampled measurement error is the output of the analog anti-aliasing chain and satisfies $|n(t)| \leq n_{\max}$. Load transitions are consequently interpreted as fast but finite-slope changes, which is consistent with the bandwidth of the electronic load and data-acquisition chain.

Definition 1 (practical voltage regulation): The output is practically regulated if, for every admissible initial condition in the set $\mathcal{X}$, all closed-loop signals remain bounded and the voltage error $e_v = v_o - v_r$ enters a computable neighborhood of the origin whose radius is determined by the observer error and any persistent applied-versus-commanded duty mismatch. The neighborhood collapses to the origin when the observer inputs vanish, and the duty projection becomes asymptotically inactive. The control problem is to construct an output-feedback law that satisfies Definition 1 throughout $\mathcal{X}$, rejects load and source disturbances represented by d, respects $\mathcal{D}$, and avoids injecting a discontinuous sign function into the pulse-width modulator. The design below addresses these requirements through a second-order LESO, an integral sliding coordinate, and a smooth super-twisting action.

3. LESO–ISTSMC DESIGN AND STABILITY ANALYSIS

The proposed linear extended-state observer-assisted integral super-twisting sliding-mode controller is abbreviated as LESO–ISTSMC. The adjective integral refers to the voltage-error coordinate in (10), while the super-twisting core is regularized by the hyperbolic tangent to obtain a continuous switching contribution to the duty command. The architecture is not a mere juxtaposition of an observer and a sliding-mode law. The applied duty is used consistently in the LESO, the duty mismatch is returned through a model-scaled anti-windup path, and the same smooth switching map is retained in both super-twisting channels. These three choices yield the triangular closed-loop structure and exact cross-term cancellation established below for the averaged sliding dynamics. The canonical channel (5) requires only a second-order observer. This is materially different from appending an additional state to an assumed second-order voltage model: the observer order follows directly from the relative degree of the averaged output channel. Define the innovation $\varepsilon_o = y_m - \hat{z}_1$ and select two distinct positive observer poles p_1 and p_2. The LESO is as in (6).

$$\dot{\hat{z}}_1 = b_n D_a + \hat{z}_2 + \ell_1 \varepsilon_o, \quad \dot{\hat{z}}_2 = \ell_2 \varepsilon_o, \quad \ell_1 = p_1 + p_2, \quad \ell_2 = p_1 p_2. \tag{6}$$

Where $\hat{z}_1$ and $\hat{z}_2$ are the estimates of the output voltage and total output-channel disturbance, respectively, and ℓ_1, ℓ_2 are the observer gains. Distinct poles provide independent pole shaping without imposing the repeated-pole parameterization used in conventional bandwidth-form LESOs. The measured input in (6) is D_a, not the unconstrained command, so actuator clipping is not misinterpreted as an external disturbance.

Let $\hat{z} = [\hat{z}_1, \hat{z}_2]^{\mathrm{T}}$ and $\tilde{z} = z - \hat{z}$ denote the observer state and estimation error, respectively. Subtraction of (6) from (5) yields (7).

$$\dot{\tilde{z}} = A_o \tilde{z} + B_h h - L_o n, \quad A_o = \begin{bmatrix} -\ell_1 & 1 \\ -\ell_2 & 0 \end{bmatrix}, \quad B_h = \begin{bmatrix} 0 \\ 1 \end{bmatrix}, \quad L_o = \begin{bmatrix} \ell_1 \\ \ell_2 \end{bmatrix}. \tag{7}$$

Where A_o is the observer-error matrix, B_h is the disturbance-rate channel, and L_o is the noise-injection vector. Because $\tilde{z}_1$ and $\tilde{z}_2$ have different physical units, the stability analysis is conducted in scaled coordinates. Select fixed base quantities $V_b > 0$ and $T_b > 0$, define $S = \mathrm{diag}(V_b^{-1}, T_b V_b^{-1})$ and $z_s = S\tilde{z}$, and set $A_s = SA_oS^{-1}$, $B_s = SB_h$, and $L_s = SL_o$. Both components of z_s are dimensionless, and A_s is similar to A_o and therefore has the same eigenvalues. Moreover, $|\tilde{z}_1| = V_b|z_{s,1}| \le V_b \parallel z_s \parallel$, which permits a voltage-dimensioned observer bound to be recovered from the scaled analysis. Throughout the analysis, $\|\cdot\|$ denotes the Euclidean vector norm applied to the scaled coordinates and its induced matrix norm.

- Lemma 1 (LESO input-to-state bound)

Under Assumption 2 and $p_1, p_2 > 0$, the scaled estimation error z_s is uniformly ultimately bounded. Consequently, the physical voltage-estimation error $\tilde{z}_1$ is uniformly ultimately bounded. Both z_s and $\tilde{z}$ converge exponentially to zero when $h = n = 0$, and converge asymptotically to zero whenever $h(t) \to 0$ and $n(t) \to 0$.

- Proof

With r denoting the characteristic variable, the characteristic polynomial of A_o is $(r + p_1)(r + p_2)$; hence A_o is Hurwitz. Because $A_s = SA_oS^{-1}$, A_s is also Hurwitz. For an arbitrary symmetric matrix $Q = Q^{\mathrm{T}} > 0$, there is a unique symmetric matrix $P = P^{\mathrm{T}} > 0$ satisfying:

$$A_s^{\mathrm{T}} P + P A_s = -Q. \tag{8}$$

where P and Q are the Lyapunov matrices. The quadratic function $V_o = z_s^{\mathrm{T}} P z_s$ satisfies $\lambda_{\min}(P) \parallel z_s \parallel^2 \le V_o \le \lambda_{\max}(P) \parallel z_s \parallel^2$. Differentiation along the scaled error dynamics gives $\dot{V}_o = -z_s^{\mathrm{T}} Q z_s + 2 z_s^{\mathrm{T}} P (B_s h - L_s n)$. Set $c_o = \parallel PB_s \parallel h_{\max} + \parallel PL_s \parallel n_{\max}$. The Cauchy–Schwarz inequality gives $\dot{V}_o \le -\lambda_{\min}(Q) \parallel z_s \parallel^2 + 2c_o \parallel z_s \parallel$; applying Young's inequality with weight $\lambda_{\min}(Q)/2$ then gives (9).

$$\dot{\mathrm{V}}_{\mathrm{o}} \le -\alpha_{\mathrm{o}} \mathrm{V}_{\mathrm{o}} + \beta_{\mathrm{o}}, \quad \limsup_{t \to \infty} \parallel z_s(t) \parallel \le \sqrt{\frac{\beta_{\mathrm{o}}}{\alpha_{\mathrm{o}} \lambda_{\min}(P)}} =: \bar{\delta}_{\mathrm{o}}, \limsup_{t \to \infty} |\tilde{z}_1(t)| \le \mathrm{V_b} \bar{\delta}_{\mathrm{o}} =: \delta_{\mathrm{v}}. \tag{9}$$

Where $\alpha_o = \lambda_{\min}(Q)/[2\lambda_{\max}(P)]$, $\beta_o = 2c_o^2/\lambda_{\min}(Q)$, $\bar{\delta}_o$ is the dimensionless scaled-error radius, and δ_v is the resulting voltage-estimation-error bound. The comparison lemma gives $V_o(t) \le e^{-\alpha_o t} V_o(0) + (\beta_o/\alpha_o)(1 - e^{-\alpha_o t})$, which proves uniform ultimate boundedness and (9). If $h = n = 0$, then $\beta_o = 0$, so the same inequality gives exponential convergence. More generally, variation of constants for the exponentially stable scaled system shows that a bounded input $B_s h - L_s n$ converging to zero produces $z_s(t) \to 0$ and, equivalently, $\tilde{z}(t) \to 0$.

- Remark 1

The (9) states the strongest conclusion supported by a linear observer under bounded disturbance rate and measurement noise: a voltage-dimensioned ultimate bound, not finite-time exact reconstruction. Increasing p_1 and p_2 reduces the low-frequency disturbance-estimation error but increases $\parallel L_s \parallel n_{\max}$, a standard high-gain-observer tradeoff [21]. The poles should therefore be placed above the voltage-loop bandwidth and below the frequency range dominated by switching ripple. This separation, together with the continuous switching approximation introduced next, motivates the bandwidth and smoothing choices evaluated experimentally.

Define the observer-based voltage error $\hat{e}_v = \hat{z}_1 - v_r$. The integral coordinate and sliding variable are selected as in (10).

$$s = \hat{e}_v + \lambda \eta, \qquad \dot{\eta} = \hat{e}_v - \frac{b_n}{\lambda}(D_a - D_c), \qquad \lambda > 0. \tag{10}$$

Where s is the sliding variable, η is the integral state, λ is its design rate, and D_c is the unconstrained duty command. The second term in $\dot{\eta}$ is a model-consistent back-calculation term. It removes the applied-versus-commanded duty mismatch from the sliding dynamics and prevents the integral state from accumulating an unattainable control demand during saturation. For a smoothing width $\phi > 0$, defined as (11).

$$\chi_\phi(s) = \tanh\left(\frac{s}{\phi}\right), |\chi_\phi(s)| < 1, s\chi_\phi(s) > 0 \ (s \neq 0), |s| \geq s_\phi \Rightarrow |\chi_\phi(s)| \geq \rho_0, s_\phi = \phi \text{artanh}(\rho_0), \quad (11)$$

Where χ_ϕ is the continuous switching function; the smoothing width ϕ has the same physical unit as the sliding variable; $\rho_0 \in (0,1)$ is an arbitrary comparison level, and s_ϕ is the corresponding boundary-layer width. These properties follow from the oddness and strict monotonicity of the hyperbolic tangent. Figure 2 makes the design tradeoff explicit: a smaller ϕ approaches the ideal sign function, whereas a larger ϕ lowers noise amplification at the cost of a wider transition layer. The integral smooth super-twisting action is generated by (12).

$$v = -k_1|s|^{1/2}\chi_\phi(s) + \xi, \quad \dot{\xi} = -k_2\chi_\phi(s), \quad k_1 > 0, \quad k_2 > 0, \quad (12)$$

Where v is the virtual reaching action, ξ is the internal super-twisting state, and k_1, k_2 are positive gains. The two-channel structure follows the super-twisting framework [28]. Replacing both occurrences of $\text{sgn}(s)$ by the same $\chi_\phi(s)$ is deliberate: it preserves the cross-term cancellation used in the proof below, whereas smoothing only one channel would not yield the same closed-loop dissipation identity. The duty command and its hardware-consistent realization are as in (13).

$$D_c = \frac{\dot{v}_r - \lambda\hat{e}_v - \hat{z}_2 - \ell_1\varepsilon_o + v}{b_n}, \qquad D_a = \Pi_{\mathcal{D}}(D_c) := \min\{D_{\max}, \max\{D_{\min}, D_c\}\}. \quad (13)$$

Where $\Pi_{\mathcal{D}}$ is the Euclidean projection onto the admissible duty interval. The innovation term is retained in (13) because it is part of $\dot{\hat{z}}_1$; omitting it would leave a noise- and observer-dependent residual in the sliding dynamics. In implementation, D_a is also fed back to (6) and (10), so the observer and anti-windup mechanism use the duty ratio that the converter actually receives.

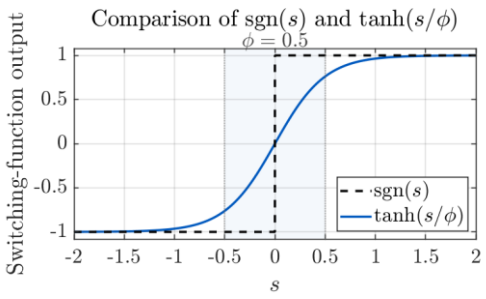

Figure 2. Comparison of $\text{sgn}(s)$ and $\tanh(s/\phi)$ for $\phi = 0.5$ V

3.1. Assumption 3 (reference feasibility)

For each constant commanded voltage in the stated operating range, the averaged converter possesses an equilibrium $(x^\star, D^\star)$, with $x^\star$ in the interior of $\mathcal{X}$ and $D^\star$ in the interior of $\mathcal{D}$. Its duty margin $\mu_D := \min\{D^\star - D_{\min}, D_{\max} - D^\star\}$ is strictly positive. This condition is necessary for zero steady-state tracking error because no controller can regulate an equilibrium that requires an inadmissible duty ratio; transient activation of the projection is handled explicitly by (10).

- Theorem 1 (practical closed-loop regulation)

Consider the averaged model (1)–(5) on the admissible set $\mathcal{X}$ under Assumptions 1–3. Apply the LESO (6), integral coordinate (10), smooth super-twisting law (12), and projected duty command (13), with $p_1, p_2, \lambda, k_1, k_2, \phi > 0$. Then:

(i) The autonomous sliding subsystem is globally asymptotically stable;
(ii) The duty constraint is satisfied for all time;
(iii) Conditional on the positive invariance of $\mathcal{X}$ stated in Assumption 1, all signals in the regional closed loop are bounded; and

(iv) With Δ_D^∞ denoting the limit superior of $|D_a(t) - D_c(t)|$, the limiting superior of $|e_v(t)|$ does not exceed $\delta_v + |b_n|\Delta_D^\infty/\lambda$. If the projection is asymptotically inactive, this bound reduces to δ_v; if, in addition, $h(t) \to 0$ and $n(t) \to 0$, then $e_v(t) \to 0$.

- Proof

Differentiate s in (10) and substitute (6). The applied-duty mismatch contributed by $\dot{\hat{z}}_1$ is exactly cancelled by the back-calculation term in $\dot{\eta}$, giving $\dot{s} = \hat{z}_2 + \ell_1\varepsilon_o - \dot{v}_r + \lambda\hat{e}_v + b_n D_c = \nu$ after (13) is inserted. Thus, the reference, observer, nominal input, and projection terms are removed algebraically rather than bounded conservatively. Consequently, the sliding subsystem and a radially unbounded candidate function are given by (14).

$$\dot{s} = -k_1|s|^{1/2}\chi_\phi(s) + \xi, \quad \dot{\xi} = -k_2\chi_\phi(s), \quad V_s = k_2\phi \mathrm{lncosh}\left(\frac{s}{\phi}\right) + \frac{1}{2}\xi^2. \tag{14}$$

Where V_s is positive definite and proper because $\mathrm{lncosh}(s/\phi)$ is nonnegative, vanishes only at $s = 0$, and grows linearly with $|s|$. Along (14), the cross terms cancel exactly:

$$\dot{V}_s = k_2\chi_\phi(s)\dot{s} + \xi\dot{\xi} = -k_1k_2|s|^{1/2}\chi_\phi^2(s) \le 0. \tag{15}$$

The set on which $\dot{V}_s = 0$ is $s = 0$. On this set, (14) gives $\dot{s} = \xi$; hence its largest invariant subset is the singleton $(s, \xi) = (0,0)$. Moreover, the map $|s|^{1/2}\tanh(s/\phi)$ is locally Lipschitz, including at the origin because it is $O\left(|s|^{3/2}\right)$ there. Thus (14) has unique maximal solutions. Every such solution remains in a compact sublevel set of the proper, nonincreasing function V_s, and is therefore forward complete. LaSalle's invariance principle gives $(s, \xi) \to (0,0)$, proving (i). It remains to verify that the auxiliary states and the physical tracking error inherit this result without presuming that saturation disappears. From (14)–(15), s, ξ, and hence ν, are bounded. The projection gives $D_a \in \mathcal{D}$ identically, which proves (ii). Assumptions 1 and 2 imply bounded z_1, $z_2 = d$, and n; Lemma 1 then gives bounded z_s and therefore bounded $\tilde{z}$, $\hat{z}$, and ε_o. The (13) consequently gives bounded D_c, so $D_a - D_c$ is bounded. Finally, (10) can be written as $\dot{\eta} = -\lambda\eta + s - (b_n/\lambda)(D_a - D_c)$. This stable scalar equation yields bounded η, and all remaining converter states are bounded by the positive invariance of $\mathcal{X}$. This step invokes, rather than proves, the regional invariance postulated in Assumption 1. Hence the regional closed-loop solution is forward complete and all its signals are bounded conditional on Assumption 1, establishing (iii). Variation of constants gives $\eta(t) = e^{-\lambda t}\eta(0) + \int_0^t e^{-\lambda(t-\tau)}\left[s(\tau) - (b_n/\lambda)\big(D_a(\tau) - D_c(\tau)\big)\right]d\tau$. Because $s(t) \to 0$, the limiting superior of $|\eta(t)|$ is no larger than $|b_n|\Delta_D^\infty/\lambda^2$. Since $\hat{e}_v = s - \lambda\eta$, the limiting superior of $|\hat{e}_v(t)|$ is no larger than $|b_n|\Delta_D^\infty/\lambda$. The actual error decomposes as $e_v = (z_1 - \hat{z}_1) + \hat{e}_v = \tilde{z}_1 + \hat{e}_v$; the voltage-component bound in (9) and the triangle inequality therefore establish the bound stated in (iv). If $D_a - D_c \to 0$, the same convolution gives $\eta \to 0$ and hence $\hat{e}_v \to 0$. If also $h, n \to 0$, Lemma 1 gives $z_s \to 0$ and equivalently $\tilde{z} \to 0$, so $e_v \to 0$. This completes the proof.

- Remark 2

With the smooth switching map, the super-twisting action is continuous and the sliding subsystem converges asymptotically rather than in finite time. Practical voltage accuracy depends on the LESO estimation bound, sensing quality, sampling, duty resolution, and any persistent projection residual. The smoothing parameter affects the local slope and transient reaching behavior but not the asymptotic bound in Theorem 1(iv). The stability result is regional and conditional on Assumption 1, without claiming global stabilization of the internal converter dynamics. Robustness follows from output-channel disturbance estimation, use of the applied duty ratio in the observer and anti-windup loop, and continuous dissipative sliding dynamics. Assumption 3 characterizes equilibria for asymptotically inactive projection.

4. RESULTS AND DISCUSSION

The experimental study examines steady-state voltage quality, rejection of an abrupt load change, and operation over an extended conversion range. The discussion is restricted to the tested operating region; no inference is made about duty ratios, conduction modes, or component stresses outside that region. The hardware arrangement used for the reported tests is shown in Figure 3. The controller was implemented on a Texas Instruments TMS320F28379D digital signal processor. The control algorithm was developed in MATLAB/Simulink and deployed to the target processor through automatic code generation. The power stage employed a 420 μH input inductor, 220 μF capacitors for C_a, C_b, C_2, and C_3, and a 470 μF capacitor for C_1. The main MOSFET was rated at 150 V, 104 A, whereas the rectifying diodes were rated at 600 V, 30 A. Experimental signals were digitized through the DSP ADC channels, and the real-time waveforms were

monitored using a digital oscilloscope and a laptop interface. Only the measured output voltage entered the feedback law; the applied duty ratio was internally available to the DSP, so no inductor-current measurement was required for control. The same converter, voltage-sensing path, PWM hardware, and acquisition settings were retained for LESO–ISTSMC and the CSMC baseline; only the voltage-control algorithm was changed. This common test platform is essential because switching ripple is sensitive to sampling, sensing, and modulation settings as well as to the control law. The continuous-time equations in sections 2 and 3 define the averaged design model. In the DSP realization, measured signals were sampled and the projected duty command was held by the digital PWM update; the reference steps were applied through the bounded-slope filter specified in Assumption 2. The experiments therefore evaluate the sampled implementation over the tested region without extending Theorem 1 to a general sampled-data stability claim. The current measurements were used only for performance assessment and did not enter the feedback law.

Figures 4(a)-4(f) present 5-ms steady-state records for reference voltages from 30 to 80 V. In all six cases, LESO–ISTSMC keeps the response centered on the commanded level without visible low-frequency drift. A small high-frequency component remains, and its amplitude is nearly uniform within each record. This observation is consistent with practical rather than exact regulation, although the averaged analysis does not resolve the switching waveform itself.

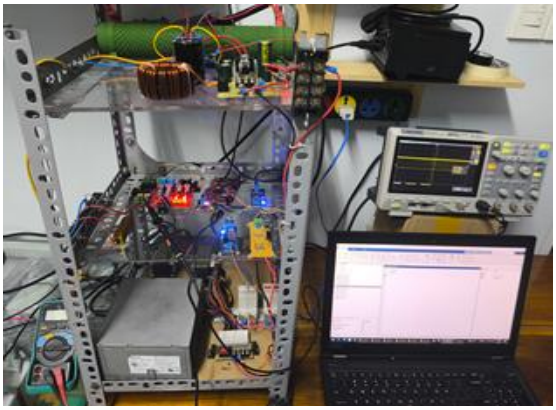

Figure 3. Experimental setup and digital control platform

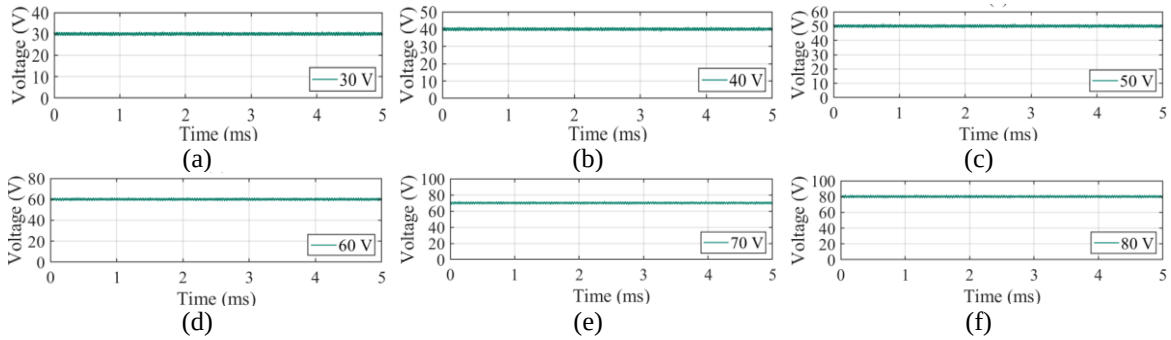

Figure 4. Steady-state output-voltage responses under LESO–ISTSMC at (a) 30 V, (b) 40 V, (c) 50 V, (d) 60 V, (e) 70 V, and (f) 80 V

The corresponding CSMC records are shown in Figures 5(a)-5(f). Although their average values remain close to the references, the traces contain a substantially wider high-frequency band. The absolute reference-centered RMS voltage deviation increases with voltage for both controllers; the normalized deviation nevertheless decreases because the reference grows faster than the residual fluctuation. This distinction prevents the apparent reduction in percentage deviation at high voltage from being misread as a reduction in its absolute magnitude. For each steady-state record, the reference-centered RMS voltage deviation was evaluated as $V_{\mathrm{rip}} = [N^{-1}\sum_{k=1}^{N}(v_o[k] - v_r)^2]^{1/2}$, and its normalized value was calculated as $r_v = 100V_{\mathrm{rip}}/v_r$, where N is the number of samples in the evaluation window. Because the deviation is formed about the reference rather than the sample mean, it contains both zero-mean ripple and any residual

steady-state bias; it is therefore a conservative voltage-quality index rather than a pure ripple-only measure. LESO–ISTSMC yields $V_{\mathrm{rip}} = 0.4769$–$0.9390$ V and $r_v = 1.1737$–1.5895% across 30–80 V. The corresponding CSMC ranges are 1.2937–2.3329 V and 2.9161–4.3125%. On a point-by-point basis, the proposed controller reduces normalized reference-centered RMS voltage deviation by 59.75–63.14%, with an average reduction of 61.23%. The mean normalized deviations are 1.3269% and 3.4370%, respectively. The reference-centered RMS voltage deviation is therefore reduced by a factor of approximately 2.5–2.7, rather than eliminated; this result is consistent with the use of $\tanh(s/\phi)$ to limit high-frequency switching activity while preserving a dissipative sliding dynamic.

Disturbance rejection was evaluated under a 50% load increase at 30, 50, and 70 V, as shown in Figure 6. LESO–ISTSMC produces voltage dips of approximately 3%, 6%, and 10%, respectively, compared with 20%, 27.5%, and 35% for CSMC, corresponding to reductions of 85.0%, 78.2%, and 71.4%. The LESO–ISTSMC responses recover through short, well-damped transients, whereas CSMC exhibits larger overshoot and low-frequency oscillations. Although disturbance rejection degrades with increasing output voltage for both controllers, the relative advantage of LESO–ISTSMC is maintained. The results are consistent with LESO-based estimation of the lumped output-channel disturbance combined with continuous super-twisting action. Because these mechanisms operate simultaneously, Figure 6 validates their composite closed-loop effect rather than their individual contributions.

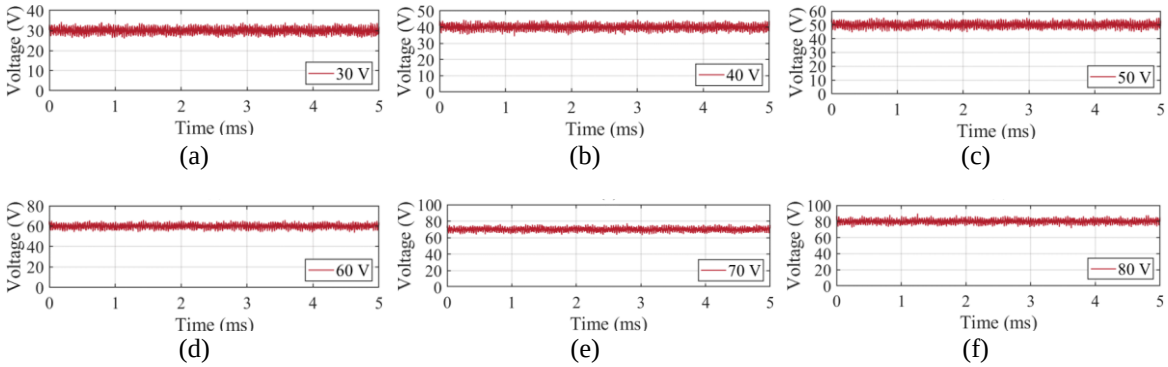

Figure 5. Steady-state output-voltage responses under CSMC at (a) 30 V, (b) 40 V, (c) 50 V, (d) 60 V, (e) 70 V, and (f) 80 V

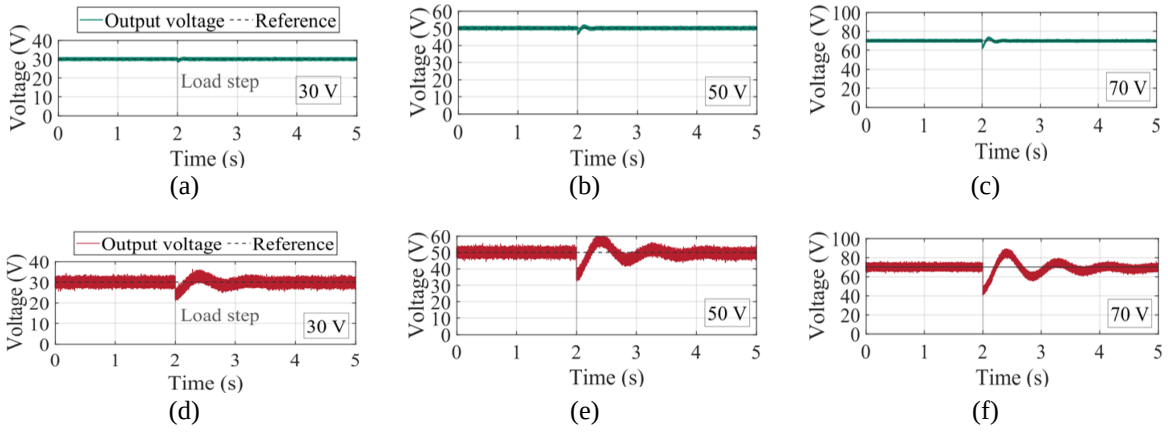

Figure 6. Output-voltage responses to a 50% load increase at $t = 2$ s: LESO–ISTSMC at (a) 30 V, (b) 50 V, (c) 70 V, CSMC at (d) 30 V, (e) 50 V, and (f) 70 V

Figures 7(a)-7(c) extend the evaluation to wide-range voltage, current, and efficiency responses, while Figure 7(d) compares the normalized RMS voltage deviation with CSMC. With the input voltage near 24 V, the output command is increased from 48 to 108 V in 12-V steps every 2 s. After each transition, the voltage and current responses settle without persistent oscillation; the input current rises from approximately 2.0 to 5.5 A, while the output current remains close to 1 A. Efficiency shows brief dips during transitions and averages 92.40% over the 12-s record. Because no paired CSMC efficiency trace is provided, Figure 7 does

not demonstrate an efficiency advantage; the valid comparison is the 59.75–63.14% reduction in normalized reference-centered RMS voltage deviation in Figure 7(d). Together, Figures 4–7 demonstrate accurate mean-voltage regulation over 30–80 V, lower steady-state ripple than CSMC, and smaller voltage excursions under a 50% load increase. The residual ripple and larger dip at 70 V are consistent with the practical regional stability of Theorem 1. Overall, the measurements support the proposed architecture within the tested range and theoretical scope of sections 2 and 3.

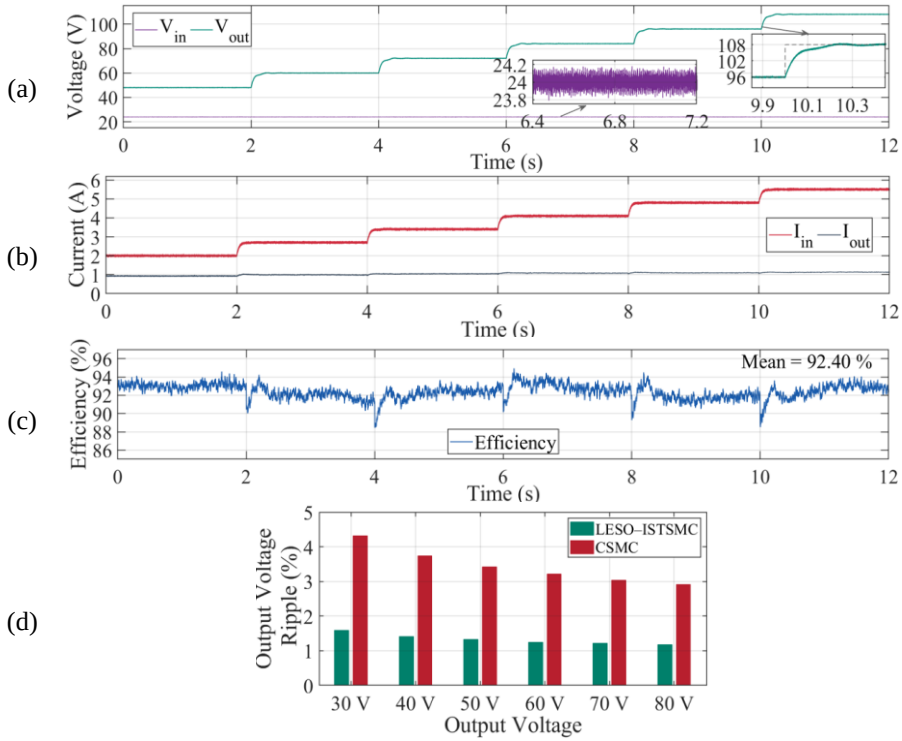

Figure 7. Wide-range performance of LESO–ISTSMC: (a) voltages, (b) currents, (c) efficiency, and (d) normalized RMS voltage deviation versus CSMC

5. CONCLUSION

Output-voltage regulation was achieved using only the measured voltage and applied duty ratio while retaining the converter's internal energy-transfer dynamics. Exact output-channel lumping allowed the LESO to estimate unmeasured-state coupling, parameter variations, and source/load disturbances through a single lumped term. Combined with tanh-regularized integral super-twisting control, duty projection, and model-consistent anti-windup feedback, the proposed scheme produced continuous duty commands and regional boundedness under Assumption 1. Compared with CSMC, normalized reference-centered RMS voltage deviation decreased by 59.75–63.14%, while load-step voltage dips were reduced by 71.4–85.0%. Stable operation from 48 to 108 V was obtained with a mean efficiency of 92.40%. These results support practical output-feedback implementation within the tested region; further validation under input-voltage transients, component aging, and conduction-mode transitions remains necessary.

FUNDING INFORMATION

Authors state no funding involved.

AUTHOR CONTRIBUTIONS STATEMENT

This journal uses the Contributor Roles Taxonomy (CRediT) to recognize individual author contributions, reduce authorship disputes, and facilitate collaboration.

Name of Author	C	M	So	Va	Fo	I	R	D	O	E	Vi	Su	P	Fu
Thanh-Lam Le	✓	✓	✓	✓	✓	✓	✓	✓	✓	✓	✓	✓	✓	✓
Nguyen Nhan Bon			✓			✓		✓	✓		✓			✓

C : **C**onceptualization
M : **M**ethodology
So : **So**ftware
Va : **Va**lidation
Fo : **Fo**rmal analysis
I : **I**nvestigation
R : **R**esources
D : **D**ata Curation
O : Writing - **O**riginal Draft
E : Writing - Review & **E**diting
Vi : **Vi**sualization
Su : **Su**pervision
P : **P**roject administration
Fu : **Fu**nding acquisition

CONFLICT OF INTEREST STATEMENT

Authors state no conflict of interest.

DATA AVAILABILITY

Data availability is not applicable to this paper as no new data were created or analyzed in this study.

REFERENCES

[1] N. B. Dişken and M. M. Savrun, "High-gain multiport DC-DC converter topologies for renewable energy applications: a comprehensive review," *Electric Power Components and Systems*, vol. 52, no. 8, pp. 1459–1473, May 2024, doi: 10.1080/15325008.2023.2287172.

[2] M. Yavari, A. Salemnia, and H. Javadi, "A new step-up DC-DC converter with high gain for photovoltaic applications," *International Journal of Circuit Theory and Applications*, vol. 51, no. 2, pp. 702–727, Feb. 2023, doi: 10.1002/cta.3447.

[3] P. Shaw, M. D. Siddique, S. Mekhilef, and A. Iqbal, "A new family of high gain boost DC-DC converters with reduced switch voltage stress for renewable energy sources," *International Journal of Circuit Theory and Applications*, vol. 51, no. 3, pp. 1265–1285, Mar. 2023, doi: 10.1002/cta.3464.

[4] R. B. Kalahasthi, M. R. Ramteke, and H. M. Suryawanshi, "A high-gain low-ripple DC–DC converter for micro-grid applications," *International Journal of Circuit Theory and Applications*, vol. 51, no. 2, pp. 807–828, Feb. 2023, doi: 10.1002/cta.3466.

[5] L. Wang, F. Zhou, P. Nie, S. Hashimoto, and T. Kawaguchi, "Dual-layer multi-port high-gain DC-DC power converter with hybrid voltage/current distribution strategy," *Electronics*, vol. 15, no. 7, Mar. 2026, doi: 10.3390/electronics15071454.

[6] I. H. Malick, M. Zaid, M. Samiullah, I. Ashraf, A. Iqbal, and A. Sarwar, "Implementation and reliability analysis of a new transformerless high-gain DC-DC converter for renewable energy applications," *Energy Storage*, vol. 5, no. 4, Jun. 2023, doi: 10.1002/est2.430.

[7] H. Nouhi, V. Talavat, and M. Farhadi-Kangarlu, "A nonisolated single-switch coupled inductor-based DC-DC converter with high voltage gain for renewable power generation systems," *International Transactions on Electrical Energy Systems*, vol. 2023, pp. 1–15, May 2023, doi: 10.1155/2023/2600232.

[8] R. B. Kalahasthi, M. R. Ramteke, H. M. Suryawanshi, and K. Kothapalli, "A single-switch high-gain DC–DC converter for photovoltaic applications," *International Journal of Circuit Theory and Applications*, vol. 50, no. 4, pp. 1194–1215, Apr. 2022, doi: 10.1002/cta.3205.

[9] L. Wu, J. Liu, S. Vazquez, and S. K. Mazumder, "Sliding mode control in power converters and drives: a review," *IEEE/CAA Journal of Automatica Sinica*, vol. 9, no. 3, pp. 392–406, Mar. 2022, doi: 10.1109/JAS.2021.1004380.

[10] A. Esmaeili and H. Gholizade-Narm, "Robust nonlinear control of a quasi-resonant DC-DC converter with turn-on and turn-off zero current switching," *IET Power Electronics*, vol. 15, no. 4, pp. 325–336, Mar. 2022, doi: 10.1049/pel2.12233.

[11] Z. Alam *et al.*, "Robust hybrid nonlinear control approach for stability enhancement of a constant power load DC-DC boost converter," *Alexandria Engineering Journal*, vol. 74, pp. 535–545, Jul. 2023, doi: 10.1016/j.aej.2023.05.041.

[12] T.-L. Le and N. N. Bon, "High-performance voltage control of ladder boost converters using robust backstepping sliding mode control," *Bulletin of Electrical Engineering and Informatics*, vol. 15, no. 2, pp. 999–1007, Apr. 2026, doi: 10.11591/eei.v15i2.11061.

[13] M. Abdolahi, J. Adabi, and S. Y. Mousazadeh Mousavi, "A passivity control and developed nonlinear disturbance observer for boost converter with constant power load in DC microgrid," *International Journal of Circuit Theory and Applications*, vol. 52, no. 11, pp. 5859–5876, Nov. 2024, doi: 10.1002/cta.4042.

[14] B. K. Insafmal and Y. Che, "Voltage control of floating interleaved boost converter using non-singular terminal sliding mode control algorithm for fuel cell systems," *Discover Electronics*, vol. 2, no. 1, Jun. 2025, doi: 10.1007/s44291-025-00076-9.

[15] D. A. Palash, T. K. Roy, Z. Alam, and A. M. T. Oo, "Design and experimental validation of a composite FRL-NFTISMC and BSC for DC-bus voltage stabilization in CPL-based DC microgrids," *IET Power Electronics*, vol. 18, no. 1, Jan. 2025, doi: 10.1049/pel2.70012.

[16] S. Oucheriah and A. Azad, "Current-sensorless robust sliding mode control for the DC-DC boost converter," *AIMS Electronics and Electrical Engineering*, vol. 9, no. 1, pp. 46–59, 2025, doi: 10.3934/electreng.2025003.

[17] J. Linares-Flores *et al.*, "Sliding mode control based on linear extended state observer for DC-to-DC buck–boost power converter system with mismatched disturbances," *IEEE Transactions on Industry Applications*, vol. 58, no. 1, pp. 940–950, Jan. 2022, doi: 10.1109/TIA.2021.3130017.

[18] O. O. Babayomi, Z. Zhang, Z. Li, and K.-B. Park, "Bidirectional DC-DC converters for distributed energy resources: Robust predictive control with structurally-adaptive extended state observers," *International Journal of Electrical Power & Energy Systems*, vol. 158, Jul. 2024, doi: 10.1016/j.ijepes.2024.109913.

[19] X. Yu, W. Chen, F. Wang, D. Ke, L. Xu, and J. Rodriguez, "Model-free predictive control of non-isolated two-stage AC–DC–DC converter based on linear extended state observer," *International Journal of Robust and Nonlinear Control*, vol. 35, no. 7, pp. 2642–2657, May 2025, doi: 10.1002/rnc.6468.
[20] M. M. Raja and Q. Zhao, "Adaptive Takagi–Sugeno (T–S) fuzzy observer based fault tolerant control for DC–DC converters with robustness against uncertainties," *The Journal of Engineering*, vol. 2024, no. 6, Jun. 2024, doi: 10.1049/tje2.12404.
[21] J. A. Gonzalez-Prieto and A. F. Villaverde, "Smooth non linear high gain observers for a class of dynamical systems," *IEEE Access*, vol. 10, pp. 3693–3704, 2022, doi: 10.1109/ACCESS.2021.3137650.
[22] Z. Xia, X. Yu, X. Wu, and Y. Dou, "An enhanced linear extended state observer-based sensorless IPMSM drives with robustness against current measurement offset error," *IEEE Transactions on Transportation Electrification*, vol. 11, no. 1, pp. 3558–3567, Feb. 2025, doi: 10.1109/TTE.2024.3443809.
[23] Y. Zheng, H.-T. Zhang, Z. Yu, X. Huang, H. Jiao, and H. Ding, "Adaptive sliding mode control with linear extended state observer for active magnetic bearing-rotor systems," *IEEE/CAA Journal of Automatica Sinica*, vol. 12, no. 8, pp. 1736–1738, Aug. 2025, doi: 10.1109/JAS.2024.125037.
[24] A. Alessandri and R. G. Sanfelice, "Switched-gain observers for linear systems by using max/min Lyapunov functions," *IEEE Control Systems Letters*, vol. 9, pp. 336–341, 2025, doi: 10.1109/LCSYS.2025.3572072.
[25] I. Aliskan, "The fractional-order proportional-integral-derivative controller tuned with hybrid particle swarm optimization-Artificial Bee Colony algorithm for boost converters: an experimental study," Arabian Journal for Science and Engineering, vol. 51, no. 16, pp. 19601–19618, Aug. 2026, doi: 10.1007/s13369-026-11423-7.
[26] C. Wang, X. Li, M. Yao, Y. Niu, and Q. Wu, "Generalized super-twisting sliding mode controller for DC-DC buck converters based on a finite-time extended state observer," *Asian Journal of Control*, Sep. 2025, doi: 10.1002/asjc.3872.
[27] J. Sun, J. Wang, A. Wen, and Z. Wang, "An integrated disturbance observer-based adaptive smooth gain sliding mode control for DC/DC converters in DC microgrids," *Electronics*, vol. 15, no. 3, Feb. 2026, doi: 10.3390/electronics15030668.
[28] G. V. Hollweg, P. J. D. de Oliveira Evald, R. V. Tambara, and H. A. Gründling, "A robust adaptive super-twisting sliding mode controller applied on grid-tied power converter with an LCL filter," *Control Engineering Practice*, vol. 122, May 2022, doi: 10.1016/j.conengprac.2022.105104.
[29] T. T. Waghmare and P. Chaturvedi, "Super twisting approach of a higher order sliding mode controller for a flyback DC–DC converter in photovoltaic applications," *International Journal of Circuit Theory and Applications*, vol. 51, no. 9, pp. 4202–4219, Sep. 2023, doi: 10.1002/cta.3636.
[30] J. Davila, M. Tranninger, and L. Fridman, "Finite-time state observer for a class of linear time-varying systems with unknown inputs," *IEEE Transactions on Automatic Control*, vol. 67, no. 6, pp. 3149–3156, Jun. 2022, doi: 10.1109/TAC.2021.3096863.

BIOGRAPHIES OF AUTHORS



Thanh-Lam Le received his M.S. degree in electrical engineering from Ho Chi Minh City University of Technology, Vietnam, and his Ph.D. degree in electrical engineering from National Cheng Kung University, Tainan, Taiwan. He is currently a lecturer in the Faculty of Electrical and Electronics Engineering at Ho Chi Minh City University of Technology and Engineering, Vietnam. His research interests include motor drives, energy conversion systems, and advanced control theory and its applications. He can be contacted at email: lamlethanh@hcmute.edu.vn.



Nguyen Nhan Bon is a graduate of Ho Chi Minh City University of Technology, Vietnam, where he received his Ph.D. degree in electrical engineering. He is currently a lecturer in the Faculty of Electrical and Electronics Engineering at Ho Chi Minh City University of Technology and Engineering, Vietnam. His research interests include power systems, transmission grid troubleshooting, and optimization algorithms. He can be contacted at email: bonnn@hcmute.edu.vn.